INTERNATIONAL JOURNAL of RENEWABLE ENERGY RESEARCH
M. Ghodbane-Cherif et al., Vol.16, No.2, June, 2026

# Enhancing Efficiency of DC-based DFIG Wind Turbines in Bipolar Micro-Grid Environments with Real-Time Validation

Meriem Ghodbane-Cherif*‡, Marwa Ben Saïd-Romdhane**,

Sondes Skander-Mustapha ***, Ilhem Slama-Belkhodja ****

*,**,***,**** Université de Tunis El Manar, Ecole Nationale d'Ingénieurs de Tunis, LR11ES15 Laboratoire de Systèmes Electriques, 1002, Tunis, Tunisie

** Université de Gabès, Institut Supérieur des Sciences Appliquées et de Technologie de Gabès, 6029 Gabès, Tunisie

*** Université de Carthage, Ecole Nationale d'Architecture et d'Urbanisme, 2026, Sidi Bou Said, Tunisie

(meriem.ghodbane@enit.utm.tn, marwa.bensaïdromdhane@enit.utm.tn, sondes.skander@enit.utm.tn, ilhem.slamabelkhodja@enit.utm.tn)

‡Corresponding Author; Meriem Ghodbane-Cherif, Université de Tunis El Manar, Ecole Nationale d'Ingénieurs de Tunis, LR11ES15 Laboratoire de Systèmes Electriques, 1002, Tunis, Tunisie, Tel: +216 98379585, meriem.ghodbane@enit.utm.tn

*Received: 26.02.2024 Accepted: 14.04.2024*

**Abstract-** This article introduces an improved regulation strategy for DC wind power systems linked to an imbalanced bipolar DC micro-grid. The study focuses on two distinct wind systems, each one connected to a separate terminal of the bipolar DC micro-grid and tested with varying wind speed profiles. The investigated wind systems are based on doubly fed induction generators with two voltage source converters: a rotor-side converter and a stator-side converter. The first one converter ensures the Maximum Power Point Tracking, while the second converter maintains balanced three-phase voltages on the stator side. Both converters employ predictive control algorithms. Simulations conducted using PSIM software prove the efficacy of the suggested control strategy in mitigating the impact of bipolar DC micro-grid imbalances on DC wind turbine efficiency. The system demonstrates performance even under challenging conditions, with DC bus variations reaching up to 50 %. To verify the system's precision and rapid dynamic response, the suggested control is compared with conventional resonant control through real-time simulations. A comparative analysis of the results demonstrates the superior suggested control efficiency for the studied system.

**Keywords** Bipolar DC micro-grid, doubly fed induction generator, wind power generation, voltage imbalance, predictive control, real-time validation.

## 1. Introduction

Recently, the electric power transmission network has undergone significant changes and high-voltage direct current (HVDC) transmission has attracted notice due to its effectiveness in delivering power over long distances. However, the generation of harmonics in converters necessitates the incorporation of both AC and DC filters, thereby leading to an increase in the cost [1-4]. Therefore, Medium Voltage Direct Current (MVDC) grids have garnered worldwide attention as a promising technology for enhancing and modernizing power distribution systems, aiming to achieve heightened reliability, flexibility, and efficiency. Such system provides reduced power losses and cables of a more compact size, all while maintaining a higher power capacity [5-8].

With the growing trend towards MVDC, there is a rising interest in the expansion of DC wind turbines today. When several researchers are interested in studying different configurations of wind farms for various purposes and under diverse conditions [9-12], others are attracted by control

strategies for DC wind Farms. In [13], the authors suggest a solution featuring electrical isolation and self-starting capabilities. The paper presents designed topologies for a DC wind turbine, a medium-voltage DC/DC converter, and a high-voltage DC/DC converter, along with their corresponding steady-state control strategies. The authors of [14] present a topology for an MMC-DC/DC converter for an offshore DC wind Power system, accompanied by the development of its comprehensive control strategy. A current-limiting approach, which involves adjusting the bridge arm voltage reference value and integrates both inner-loop and outer-loop control mechanisms is given in [15]. In [16], researchers introduce a topological layout of a parallel all-DC wind power system featuring a turbine-side boost, grounded on a novel DC conversion method.

Ensuring DC-link stability represents one of the current challenges faced by researchers and several works treat fault tolerant control to stabilize the DC-link voltage [17-23]. The authors of [17], for example, introduce a control strategy utilizing the Lyapunov function, ensuring global asymptotic stability, is applied to the bidirectional converter managing the battery and supercapacitor. This method aims to maintain a constant DC link voltage even under varying conditions like solar and wind oscillations and changes in the load.

This paper focuses on wind turbine control within a Bipolar Direct Current Micro-Grid (BDCMG), utilizing a doubly fed induction generator (DFIG). The adopted configuration, characterized by three DC lines, demonstrates a superior level of reliability and effectiveness compared to unipolar micro-grids [24-26]. Although, the imbalance of BDCMG connections is a genuine trouble caused by operational variations of devices connected to distinct terminals. [27-29].

The proposed enhanced approach ensures MPPT regardless of the Bipolar Direct Current Micro-Grid state. The regulatory algorithm leverages a Dead-Beat predictive strategy, ensuring superior performance during transients by placing system poles at zero, thereby enhancing response speed and accuracy. This requires a brief sampling interval for precise control, ensuring minimal error, swift changes, and rapid system response. Advances in microprocessor technology have overcome the challenge of high computation requirements.

The key objective of this paper is to design an effective DC wind system control in the case of an imbalanced bipolar DC micro-grid, emphasizing fast response and accuracy. The paper is structured as follows: an outline of DFIG DC wind structures is provided in section 2, followed by system modeling in section 3. Rotor and stator side converter regulations are investigated in sections 4 and 5, and section 6 presents simulation results and their discussion. Finally, real-time validation results are presented to validate the proposed control in section 7.

## 2. DC Based DFIG Wind Turbines Configurations

Three primary configurations of DFIG-based DC wind systems are illustrated in Fig. 1. The first option, explored in [30], involves incorporating an AC/DC converter to connect between the DC micro-grid and the conventional DFIG wind system as presented in Fig. 1.*a*. The rotor side power converter control is comparable to the case of AC grid-connected wind system. However, this topology encounters challenges due to the significant quantity of power converters involved, leading to associated complexities.

References [31] and [32] suggested a second configuration that centers around a DFIG with both rotor and stator linked to the DC bus through a voltage-source inverter (VSI) and a rectifier diode, respectively, as presented in Fig. 1.*b*. The rotor side converter control assumes the stator frequency. Nonetheless, this structure results in a rise in the stator current total harmonic distortion.

In [33], the authors propose a multiple reference frame method to mitigate torque ripples, based on the topology illustrated in Fig. 1.*b*.

A third option involves interfacing the DC link with the DFIG using two VSI, as depicted in Fig. 1.*c*. One converter resides on the stator side, while the other is positioned on the rotor side. Utilizing a VSI on the stator side enables precise control of stator frequency and voltage, ensuring enhanced operational stability of the wind system [34-35]. Power generation regulation is achieved through rotor control on the converter side.

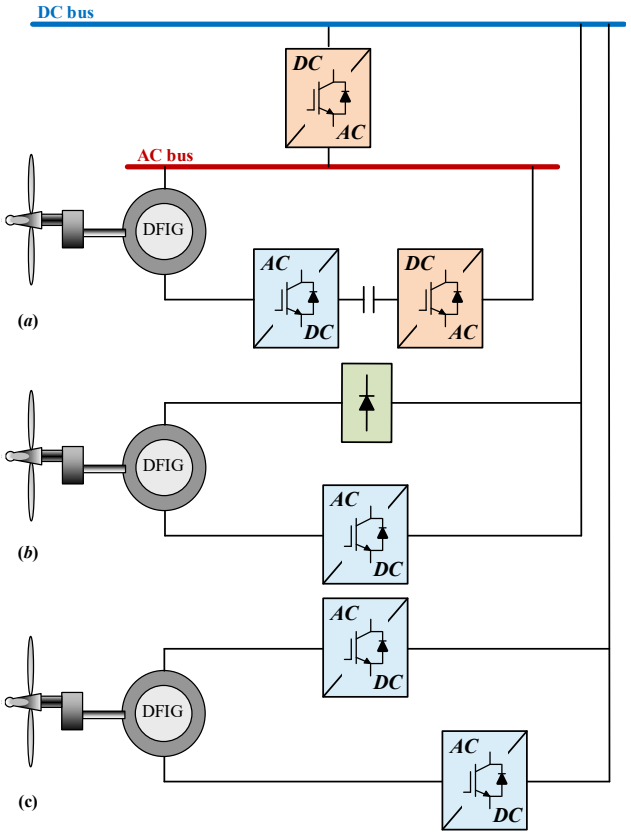


**Fig. 1.** Different DC wind turbines configurations with DFIG.

The configuration depicted in Fig. 1.*c* has previously been utilized in DFIG-based wind systems linked to the AC grid [36]. Notably, this topology offers improved power distribution between the stator and the rotor in such cases.

Interconnecting multiple wind turbine units is a crucial aspect, with parallel or series connections being common in DC networks. Fig. 2 illustrates the potential combinations.

In this study, the configuration illustrated in Fig .1.*c*, which includes two voltage source inverters, is adopted. This selection offers increased flexibility while minimizing the required quantity of power converters.

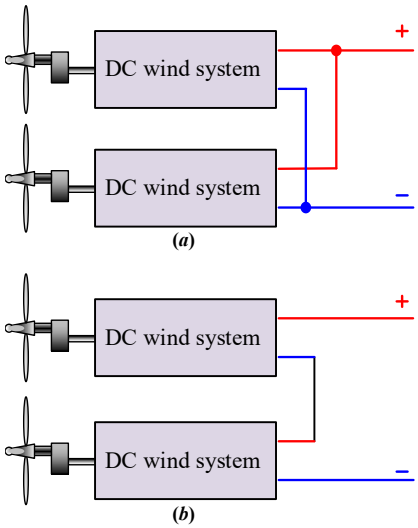


**Fig. 2.** DC micro-grid connecting wind turbines configurations (*a*) in parallel, (*b*) in series.

## 3. Modeling of DC Wind Systems with DFIG

The depicted system is shown in Fig.3, wherein two DC-connected DFIG wind systems, sharing similar configurations, are connected to distinct terminals of the BDCMG. Each system is linked to DC bus through two power converters: the Stator Side Converter (SsC) facilitates communication of the DC bus with the stator, while the Rotor Side Converter (RsC) connects the rotor to the DC bus.

A DFIG dynamic model is introduced in equation (1), where Vs representing stator voltage and $V_r$ representing rotor voltage [37-41].

$$\begin{cases} \overrightarrow{V_s} = j\omega_s \overrightarrow{\varphi_s} + \frac{d\overrightarrow{\varphi_s}}{dt} + R_s \overrightarrow{i_s} \\ \overrightarrow{V_r} = j\omega_r \overrightarrow{\varphi_r} + \frac{d\overrightarrow{\varphi_r}}{dt} + R_r \overrightarrow{i_r} \end{cases} \quad (1)$$

where is the space vector complex component. The inductances $L_m$, $L_s$, $L_r$ are, respectively, mutual, stator and rotor cyclic inductances and $R_r$ and $R_s$ are stator and rotor resistances. Equation (2) gives the fluxes of the rotor and stator.

$$\begin{cases} \overrightarrow{\varphi_s} = L_s \overrightarrow{i_s} + L_m \overrightarrow{i_r} \\ \overrightarrow{\varphi_r} = L_m \overrightarrow{i_s} + L_r \overrightarrow{i_r} \end{cases} \quad (2)$$

Fig.4 details the methodology followed throughout the paper to develop and validate the proposed configuration and control.

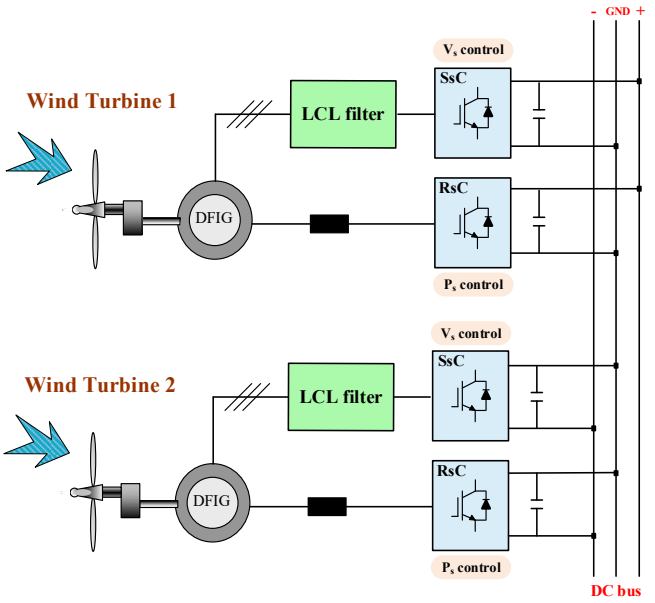


**Fig. 3.** Incorporation of bipolar DC micro-grid with two DFIG systems

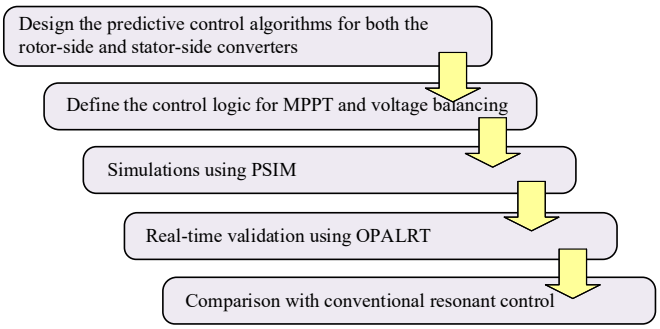


**Fig. 4.** Methodology overview for validation of proposed configuration and control.

## 4. RsC Regulation

The regulation of the RsC, depicted in Fig. 5, relies on a predictive algorithm for rapid dynamic responses. The stator flux vector is synchronized with *dq* reference frame, leading to a null q-component of the stator flux vector and allowing for autonomous regulation of stator reactive and active powers. The angular frequency of the stator angle is determined based on a Second Order Generalized Integrator Phase-Locked Loop (SOGIPLL). Equation (3) outlines the predictive controller's references for the predictive controller employed in both wind turbines. The prediction criterion is formulated in (4).

$$\begin{cases} i_{r\_d\_refWT} = \frac{L_s}{L_m V_{s\_q}} \left( \frac{V_{s\_q} \varphi_{s\_d}}{L_s} - Q_{s\_ref} \right) \\ i_{r\_q\_refWT} = -\frac{L_s}{L_m V_{s\_q}} P_{s\_ref} \end{cases} \quad (3)$$

$$\begin{cases} i_{r\_d}[i+1] = i_{r\_d\_refWT}[i] \\ i_{r\_q}[i+1] = i_{r\_q\_refWT}[i] \end{cases} \quad (4)$$

Equation (5) defines the rotor voltage *dq* components, while the rotor voltage discrete equations are provided by (6).

$$\begin{cases} V_{r\_d} = \sigma L_r \dfrac{di_{r\_d}}{dt} + R_r i_{r\_d} - \omega_r \varphi_{r\_q} \\ V_{r\_q} = \sigma L_r \dfrac{di_{r\_q}}{dt} + R_r i_{r\_q} + \omega_r \varphi_{r\_d} \end{cases} \quad (5)$$

Where σ is the leakage coefficient.

$$\begin{cases} V_{r\_d}[k] = \sigma \dfrac{L_r}{Ts} i_{r\_d}[\mathrm{k+1}] + R_r i_{r\_d}[k] - \omega_r \varphi_{r\_q}[k] \\ V_{r\_q} = \sigma \dfrac{L_r}{Ts} i_{r\_q}[\mathrm{k+1}] + R_r i_{r\_q}[k] + \omega_r \varphi_{r\_d}[k] \end{cases} \quad (6)$$

The reference of the stator power is delivered using the Maximum Power Point Tracking (MPPT) algorithm based on the operational zone [32]. Its overall expression is outlined in equation (7).

$$P_{s\_ref} = \frac{1}{2} \pi \rho R^5 \Omega_{shaft}^3 \frac{C_{pmax}}{\lambda_{opt}^3} \quad (7)$$

where $\Omega_{shaft}$, $C_{pmax}$, $R$, $\lambda_{opt}$, and ρ are shaft speed, maximum power coefficient, the, turbine rotor radius, optimal tip speed ratio and the air density, respectively.

## 5. SsC Regulation

The regulation system of the SsC guarantees the regulation of alternative voltage with stable frequency and appropriate magnitude on the stator side of the DFIG, even amidst DC bus imbalances (Fig. 6).

Predictive control is employed for regulating the LCL filter capacitor voltages, as illustrated in Fig. 6. The prediction criterion is defined by equations (8).

$$V_{c\_dq}[i+1] = V_{c\_dq\_ref}[i] \quad (8)$$

The terms $V_{c\_dq}$ and $V_{c\_dq\_ref}$ refer to the LCL filter capacitor voltage and their references on the *dq* reference frame. Equation (9) illustrates the currents in the filter.

$$\begin{cases} i_s = i_c + i_{ssc} \\ i_c = C \dfrac{dV_c}{dt} \end{cases} \quad (9)$$

Where $i_s$ is the stator current, $i_{ssc}$ is the SsC current, $i_c$ is the capacitor current and C is the capacitance value. Equation (10) presents the SsC voltage.

$$V_{ssc} = -L_1 \frac{di_{ssc}}{dt} + V_c \quad (10)$$

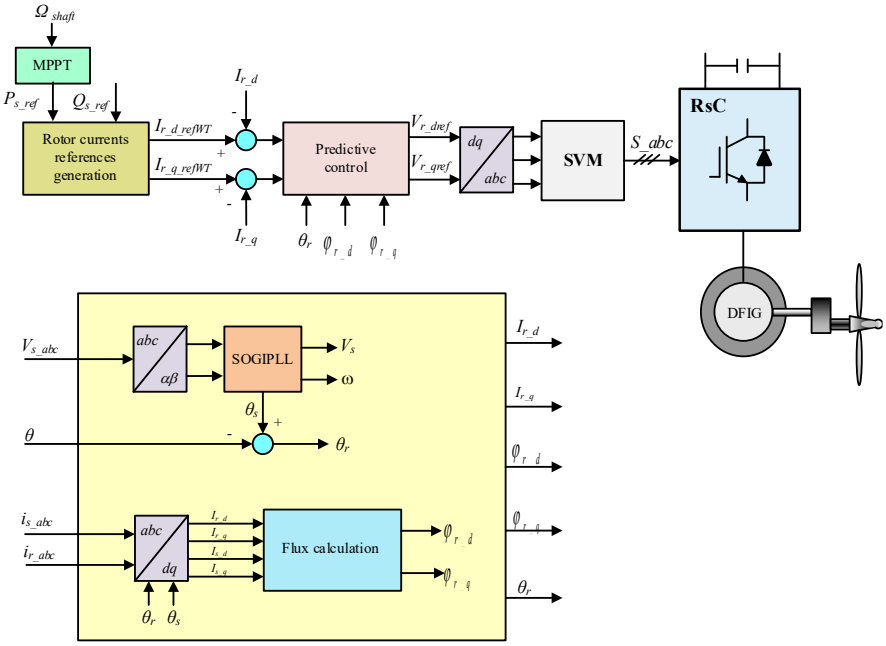


**Fig. 5.** RsC control.

$L_1$ denotes the filter inductance.

Expression (11) is derived from the previous equations.

$$V_{ssc} = -L_1 \frac{di_s}{dt} + L_1 C \frac{d^2 V_c}{dt^2} + V_c \quad (11)$$

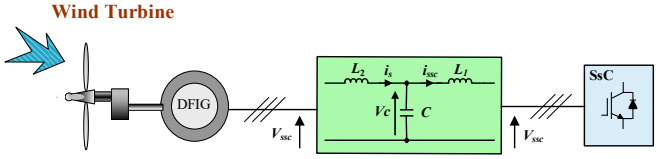


**Fig. 6.** Configuration of the LCL filter.

With the provided expression for the voltage across inductance $L_2$ in equation (12), we can infer the updated expression for $V_{SsC}$ as given in equation (13).

$$\frac{di_s}{dt}=\frac{1}{L_2}\left(V_s-V_c\right) \tag{12}$$

$$V_{ssc}=-\frac{L_1}{L_2}V_s+L_1C\frac{d^2V_c}{dt^2}+\left(1+\frac{L_1}{L_2}\right)V_c \tag{13}$$

In summary, equation (14) presents the derived expression for the differential voltage across the filter capacitor.

$$\frac{d^2V_c}{dt^2}=\frac{1}{L_1C}\left(V_{ssc}-\left(1+\frac{L_1}{L_2}\right)V_c+\frac{L_1}{L_2}V_s\right) \tag{14}$$

The differential equations for the filter capacitor voltage are subsequently provided in equation (15).

$$\begin{cases}\dfrac{d^2V_{c\_d}}{dt^2}=\dfrac{1}{L_1C}\left(V_{ssc\_d}-\left(1+\dfrac{L_1}{L_2}\right)V_{c\_d}+\dfrac{L_1}{L_2}V_{s\_d}+\omega_sCV_{c\_q}\right)\\ \dfrac{d^2V_{c\_q}}{dt^2}=\dfrac{1}{L_1C}\left(V_{ssc\_q}-\left(1+\dfrac{L_1}{L_2}\right)V_{c\_q}+\dfrac{L_1}{L_2}V_{s\_q}-\omega_sCV_{c\_d}\right)\end{cases} \tag{15}$$

Here, $V_{s\_d}$ and $V_{s\_q}$ denote the stator voltage terminals $dq$ components, while $V_{SsC}\_d$ and $V_{SsC}\_q$ represent the SsC terminals $dq$ components.

The predictive control algorithm proposed aims to synchronize the output voltage of the SsC at the $(i+2)^{th}$ sampling period with the $(i)^{th}$ sampling period reference values, reducing the discrepancy between the predicted voltage components and their references as outlined in equation (16).

$$V_{c\_dq}[i+2]=V_{c\_dq}[i+1]=V_{c\_dq\_ref}[i] \tag{16}$$

The voltage components can be represented according to equation (17).

$$V_{c\_dq}[i+2]=a\left(cV_{s\_dq}[i]-bV_{c\_dq}[i]+V_{ssc\_dq}[i]\pm\omega_sCV_{c\_qq}[i]\right) \tag{17}$$

$T_s$ represents the sampling period, and the constants $a$, $b$ and $c$ are expressed as follows.

$$a=\frac{T_s^2}{L_1C},\qquad b=1+\frac{L_1}{L_2},\qquad c=\frac{L_1}{L_2} \tag{18}$$

## 6. Analysis and Discussion of the Results

The research aim is to address the BDCMG imbalance adverse effects on the operational effectiveness of DC wind turbines. Simulation assessments are performed utilizing PSIM software, simulating a setup consisting of two wind turbines as illustrated in Fig. 3. The BDCMG is represented as an imbalanced micro-grid with varying loads linked to its terminals. Detailed specifications of the equipment can be found in Table 2 of the Appendix.

Fig. 7 illustrates the DC voltages at both terminals, Vdc1 and Vdc2, of the BDCMG. Expressed in per unit, the values highlight the extent of bus fluctuation. This study noted fluctuations in the DC bus of up to 50% under severe conditions.

Fig. 8 depicts the active power references for the wind systems provided by the MPPT modules of both turbines. Once the wind speed surpasses a predetermined threshold, it's noteworthy that the MPPT algorithm maintains a constant power output.

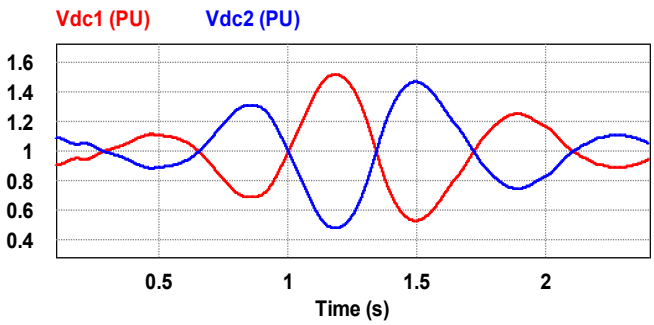


**Fig. 7.** DC micro-grid terminal voltages (p.u.).

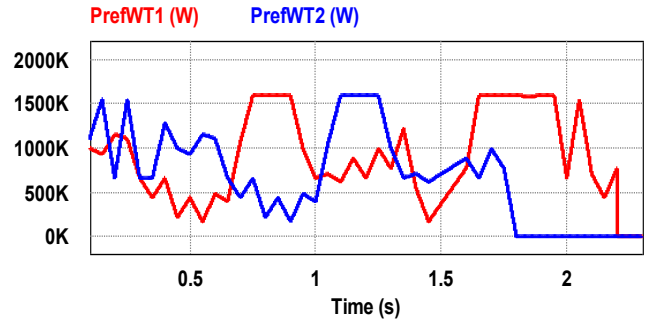


**Fig. 8.** Power references of both wind systems.

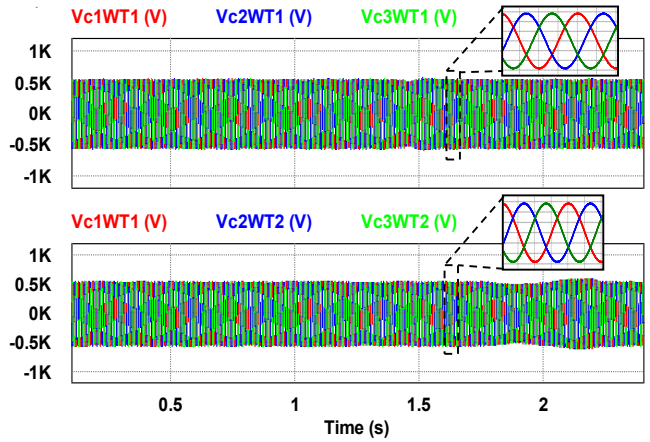


**Fig.9.** Both wind turbines three-phase stator voltage.

The wind systems' behaviors are examined within specified parameters. In Fig. 9, the two wind systems stator voltage are illustrated. The suggested control of the SsC ensures balanced voltage levels even in the presence of DC bus fluctuations. Stator currents are portrayed in Fig. 10, further magnified in Fig. 11, with fluctuations primarily

attributed to changes in wind speed rather than instability in the DC bus. The consistent 50Hz frequency of the stator current supports this observation. FFT analysis of the stator current for both turbines is presented in Fig. 12.

Fig. 13 showcases the two wind turbines rotor current, while Fig. 14 displays the FFT of rotor current. The findings depicted in Fig. 15 affirm that despite different BDCMG terminal conditions and varying wind speeds, both wind systems adeptly follow power references in the presence of an imbalanced DC bus.

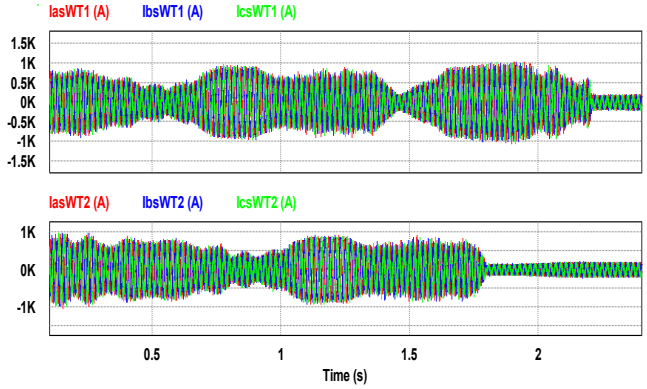


**Fig. 10.** Both wind turbines three-phase stator current.

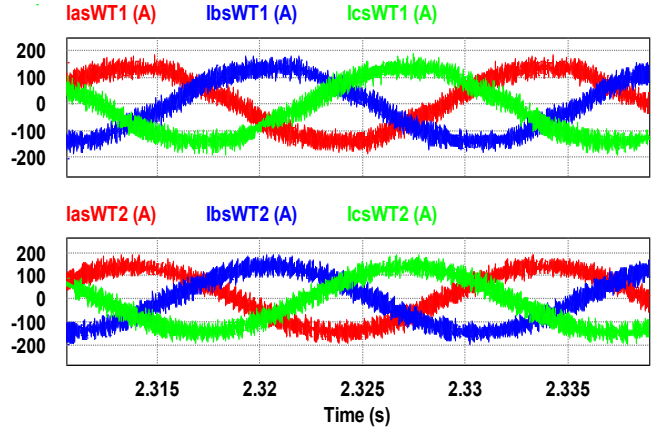


**Fig. 11.** Zoom of both wind turbines three-phase stator current.

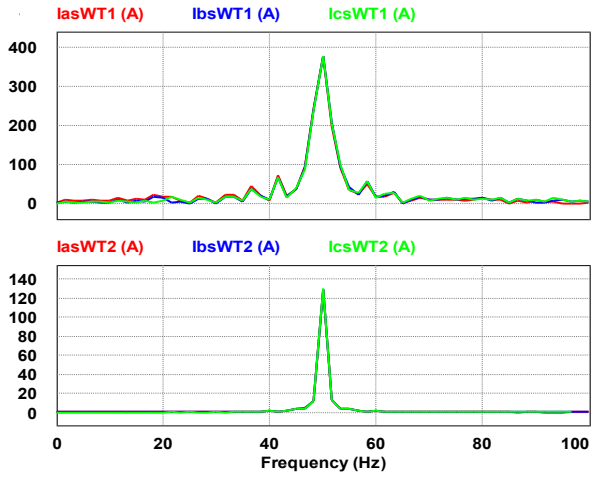


**Fig. 12.** Both wind turbines stator current FFT.

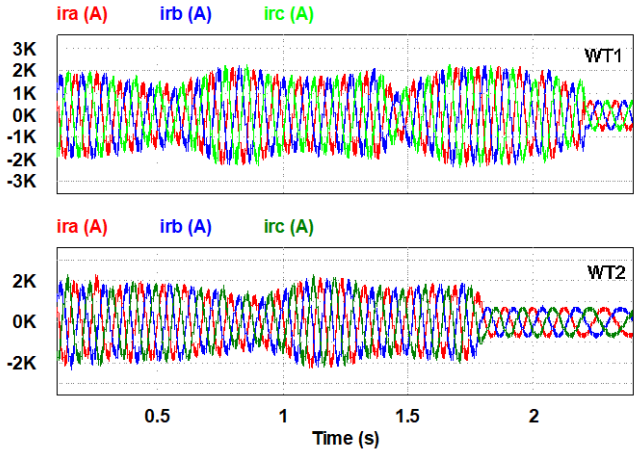


**Fig. 13.** Both wind turbines rotor current.

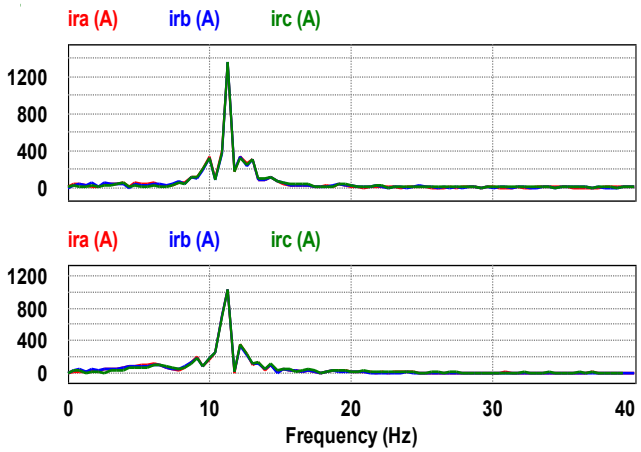


**Fig. 14.** both wind turbines rotor current FFT.

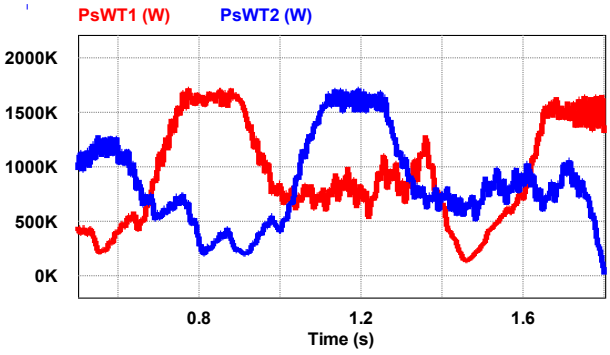


**Fig. 15.** Two wind turbines connected to a bipolar DC micro-grid supply stator power.

## 7. Real-Time Validation

The real-time validation goal is to verify the efficacy of the proposed control, applied to DC wind turbines linked to variable BDCMG, compared to conventional control.

Tests are based on a Software-the-loop platform. The model is implemented on an FPGA chip, using the RT-LAB real-time validation platform of Opal-RT 4510 with Simscape Blocksets. Simscape provides VHDL code for implementation on the Opal-RT FPGA. This enables rapid real-time model

computation on the target system while reducing scheduling overhead to under a microsecond.

The studied scheme is constituted by two identical wind systems, linked to various BDCMG terminals. Proposed control is applied to the first wind system and conventional control, based on PI controllers for RsC and Resonant Controllers (RC) for SsC, is used for the second wind system. DFIG and bipolar DC bus parameters can be found in Table 3 of the Appendix. For this test, an increase in the torque value from 15 N.m to 20 N.m is considered.

Fig. 16, Fig. 17 and Fig. 18 show the stator three-phase voltages and stator three-phase currents for both wind systems, respectively. Fig. 19 and Fig. 20 present the rotor three-phase currents and the *dq* rotor current components for both wind systems, respectively. Exposed results demonstrate that first wind system presents less harmonic distortion than second one.

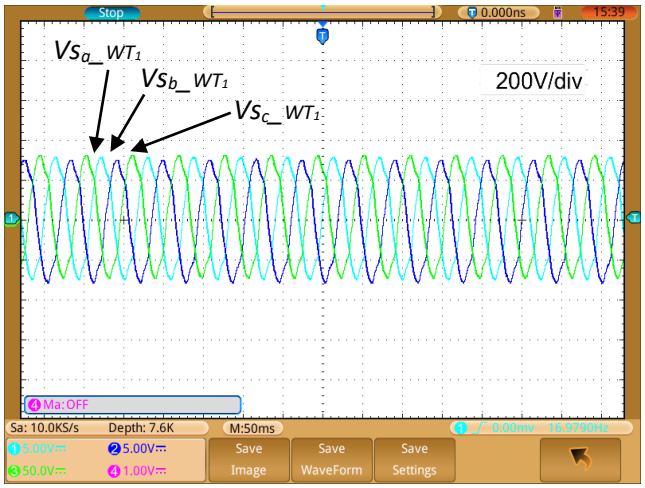


**Fig. 16.** Wind system number 1 stator three-phase voltage.

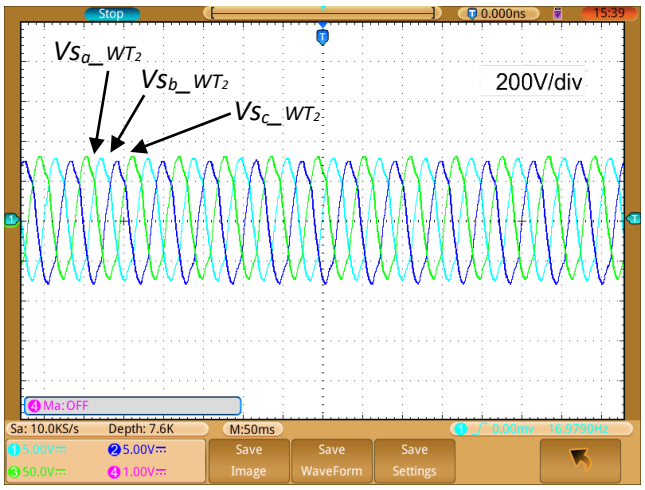


**Fig. 17.** Stator voltages of wind system number 2.

Numerical results are exposed in Table 4. Ripples of q rotor current component are significantly reduced with proposed control compared to PI control. The amount is decreased from 20% to 2%. In addition, the torque ripples presented in Fig. 21 are reduced from 30% to 8%. The total harmonic distortion (THD) analysis of stator current is reduced from 10.26% with resonant control to 4.77% with proposed control.

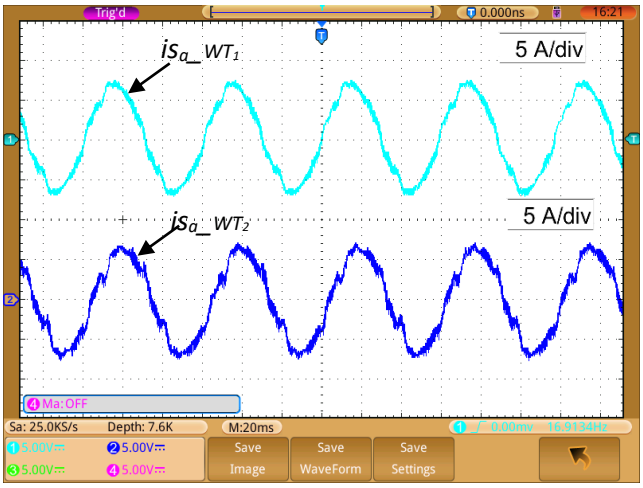


**Fig. 18.** Stator currents of both wind systems.

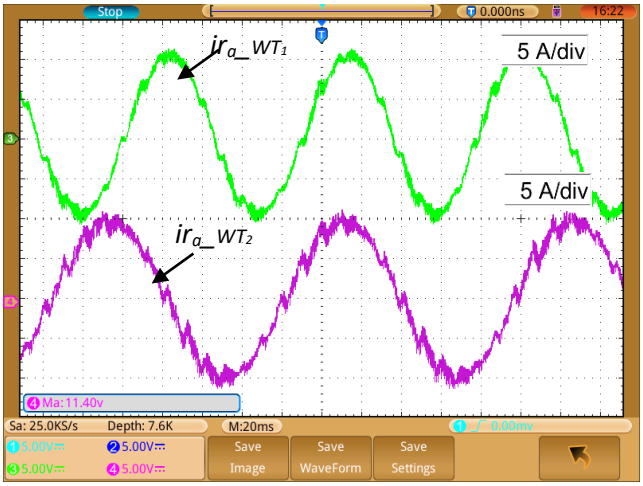


**Fig. 19.** Rotor currents of both wind systems.

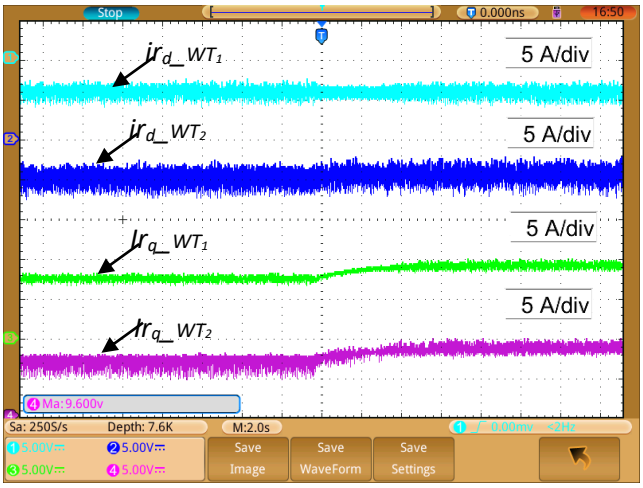


**Fig. 20.** *dq* rotor current component ($i_{rd}$, $i_{rd}$) of both wind systems.

Fig. 22 exposes Rotor current of both wind systems when wind systems pass from hypo-synchronous mode to hyper-synchronous mode. The second wind system that operates with conventional control presents a delay of 1s compared to

the first wind system. This validates the fast response and accuracy of the proposed control.

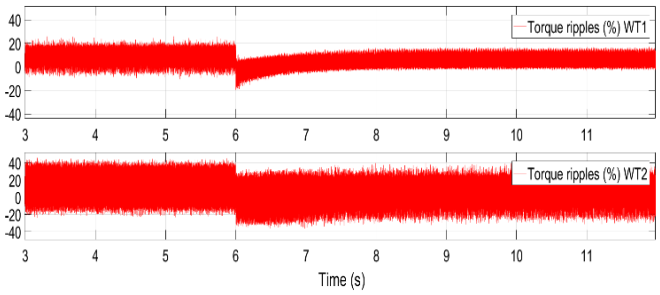


**Fig. 21.** Torque ripples in percent of both wind systems.

Table 1 provides a comparative analysis between the proposed method and the unipolar DC micro-grid (DCMG) configuration in terms of mitigation of voltage imbalance and ripples.

**Table 1.** Comparison of proposed method with unipolar DCMG

| Parameter | Mitigation of Voltage Imbalance | Ripple Percentage |
|---|---|---|
| **Proposed Method** | High effectiveness, with fluctuations up to 50% mitigated under severe conditions | Significant reduction achieved, with Q rotor current component reduced from 20% to 2%, and torque ripples decreased from 30% to 8% |
| **Unipolar DCMG** | Limited mitigation capability, with fluctuations often exceeding 50% | Higher ripple percentages observed, indicating less effective control |

Based on comparative analysis, our proposed method demonstrates superior efficiency in mitigating voltage imbalance and reducing ripple percentages compared to a unipolar DCMG configuration. Furthermore, the results align with the requirements outlined in the IEEE-1547-2018 standards, affirming the efficacy and compliance of our approach.

## 8. Conclusion

The paper introduces a control strategy for a wind turbine linked to a bipolar DC micro-grid. To ensure robust operation against DC bus fluctuations, the investigated regulation is based on predictive algorithm. Two inverters are installed in the studied system. The stator side converter is managed to maintain a stable stator voltage, while the rotor side converter is regulated for the MPPT. Simulation results are presented to illustrate the effectiveness of the proposed control. The system demonstrates performance even under challenging conditions, with DC bus variations reaching up to fifty percent. These results highlight the robustness of the control strategy in managing significant variations. Both proposed and conventional control strategies are implemented in a Software in the Loop (SIL) environment. A comparative analysis of the results demonstrates the superior suggested control efficiency for the studied system.

## 9. Future Work

Future research could explore deeper into exploring the adaptability and scalability of the proposed control strategy, potentially extending its application to larger-scale renewable energy systems and diverse environmental conditions.

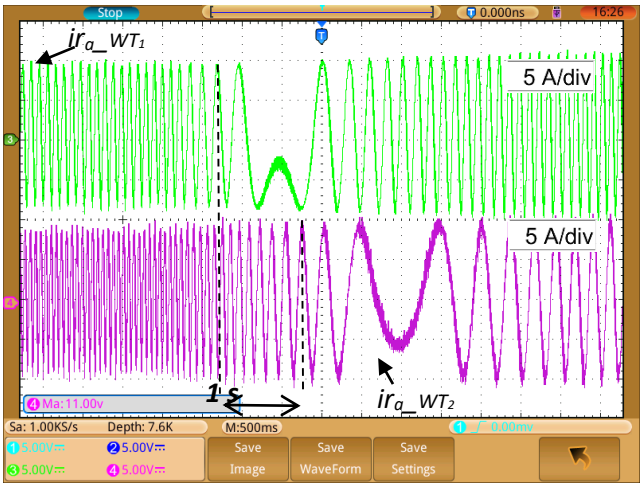


**Fig. 22.** Rotor current of both wind systems when transition from hypo-synchronous mode to hyper-synchronous mode.

## Acknowledgements

This work was supported by the Tunisian Ministry of Higher Education and Scientific Research under Grant LSE-ENIT-LR 11ES15, the research common services unit MICROGRID Platform (USCR-MGP), and by the project "Development of an Intelligent, Sustainable and Autonomous Cold Room Powered by Photovoltaic Panels (Code T3P3) " , supported by the ARESSE component of the environmental action support program "Tunisie Verte & Durable", funded by the European Union.

## Author Contributions

Meriem Ghodbane-Cherif was responsible for conceptualization, validation, resources, data curation, software development, and project administration. Meriem Ghodbane-Cherif and Marwa Ben Saïd-Romdhane jointly contributed to the methodology, formal analysis, investigation, original draft preparation, review and editing, visualization, supervision, and funding acquisition. Sondes Skander-Mustapha contributed to the investigation, data curation, visualization, and manuscript review and editing. Ilhem Slama-Belkhodja contributed to supervision, validation, and manuscript review and editing. All authors have read and agreed to the published version of the manuscript.

## Conflict of Interest

The authors declared no potential conflicts of interest with respect to the research, authorship, and/or publication of this article.

**References**

[1] M. Kim and S. H. Lee, "Numerical analysis of ion flow in one-bipole HVDC transmission line using revised charge injection methods," IEEE Access, vol. 12, pp. 22573–22581, Feb. 2024. doi: 10.1109/ACCESS.2024.3361937.

[2] F. Wang, G. Zou, H. Ding, and C. Xu, "High voltage gain three-level DC–DC converter with switched-capacitor technique for DC wind farms," IEEE Transactions on Industrial Electronics, early access. doi: 10.1109/TIE.2023.3347851.

[3] M. Wu, Y. Zhu, D. Chang, B. Hu, Y. Zhu, and W. Wu, "Research on the influence of multi-HVDC power coordinated control strategy on frequency stability in multi-partitioned power grid," 7th International Conference on Smart Grid and Smart Cities (ICSGSC), Lanzhou, China, pp. 199–204, Sept. 2023.

[4] M. V. Czernorucki, M. B. C. Salles, A. S. Melo, E. C. M. da Costa, and L. Piegari, "Effects of the HVDC system on converter transformers," 8th International Conference on Renewable Energy Research and Applications (ICRERA), Brasov, Romania, pp. 623–630, Nov. 2019. doi: 10.1109/ICRERA47325.2019.8997095.

[5] H. A. Hussain and K. A. N. Al-Deen, "Design and control of series-DC wind farms based on three-phase dual active bridge converters," IEEE Energy Conversion Congress and Exposition (ECCE), Detroit, MI, USA, pp. 1–8, Oct. 2022.

[6] Z. Cai, L. Ren, X. Tan, Z. Li, Y. Xu, Y. Tang, J. Shi, J. Li, "Study of DC superconducting current-limiting switch in MVDC shipboard power system," IEEE Transactions on Applied Superconductivity, vol. 31, no. 8, pp. 1–5, Nov. 2021. doi: 10.1109/TASC.2021.3108737.

[7] A. Clerici, R. Chiumeo, and C. Gandolfi, "MVDC multi-terminal grids: A valid support for distribution grids improvement," AEIT International Annual Conference (AEIT), Catania, Italy, pp. 1–6, Sept. 2020.

[8] I. Alhurayyis, A. Elkhateb, and D. J. Morrow, "Bidirectional DC–DC resonant converter design for electric vehicle charging stations integration to MVDC grids," 2020 9th International Conference on Renewable Energy Research and Application (ICRERA), Glasgow, UK, pp. 236–241, 2020. doi: 10.1109/ICRERA49962.2020.9242656.

[9] H. Nourmohamadi, G. Gohil, and P. T. Balsara, "Fault location and classification for MVDC networks," IEEE Journal of Emerging and Selected Topics in Power Electronics, vol. 10, no. 1, pp. 589–603, Feb. 2022. doi: 10.1109/JESTPE.2021.3111825.

[10] C. Pan, C. Hou, S. Wen, M. Zhu, and X. Kong, "Advanced topology design framework for DC offshore wind farm collection system," IEEE PELS Students and Young Professionals Symposium (SYPS), Shanghai, China, pp. 1–6, Aug. 2023.

[11] M. F. Adlinde, A. Ravi, and J. D. Sathyaraj, "Enhanced power generation and management in hybrid PV-wind microgrid with modified Z-source Zeta converter and battery storage," Electrical Engineering, 2024. doi: 10.1007/s00202-024-02263-5.

[12] K. A. Nour Al-Deen and H. A. Hussain, "Review of DC offshore wind farm topologies," IEEE Energy Conversion Congress and Exposition (ECCE), Vancouver, BC, Canada, pp. 53–60, Oct. 2021.

[13] H. Ding, G. Zou, F. Wang, and C. Xu, "Modelling and control strategies of DC offshore wind farm," IEEE 8th Asia Conference on Power and Electrical Engineering (ACPEE), Tianjin, China, pp. 1224–1228, Apr. 2023.

[14] Q. Xu, Y. Zhou, Q. Liu, X. Tian, and Z. Yuan, "MMC-DC/DC converter and its control strategy for offshore full DC wind power system," 6th International Conference on Power and Energy Applications (ICPEA), Weihai, China, pp. 171–176, Nov. 2023.

[15] T. Liang, Y. Zhang, F. Xie, and Z. Hao, "Fault current-limiting control and isolation strategy of all-DC offshore wind transmission system," 5th Asia Energy and Electrical Engineering Symposium (AEEES), Chengdu, China, pp. 587–592, Mar. 2023.

[16] H. Han, Z. Li, H. Wang, Q. Feng, R. Guo, Z. Yang, X. Liu, "Design of a parallel all-DC wind power system with turbine-side boost based on a new DC conversion," IEEE Access, vol. 12, pp. 3054–3069, 2024. doi: 10.1109/ACCESS.2023.3349294.

[17] T. Thomas, M. K. Mishra, C. Kumar, and M. Liserre, "Control of a PV-wind based DC microgrid with hybrid energy storage system using Lyapunov approach and sliding mode control," IEEE Transactions on Industry Applications, early access. doi: 10.1109/TIA.2023.3349359.

[18] W. Qin, Y. Qiu, and Y. Feng, "An improved discontinuous SVM based fault-tolerant control of AC/DC converter for all-DC offshore wind power system," CSEE Journal of Power and Energy Systems, early access. doi: 10.17775/CSEEJPES.2022.01740.

[19] A. Azizi, S. Peyghami, H. Wang, and F. Blaabjerg, "Risk evaluation of hybrid microgrids considering DC-link voltage stability," IEEE PEDG, Kiel, Germany, pp. 1–6, June 2022.

[20] S. Betamony, J. Buire, S. Bacha, T. P. Do, A. Bier, and Q. T. Tran, "Modeling and pre-installation stability assessment of a real grid-connected MV DC microgrid," IEEE ISGT Europe, Grenoble, France, pp. 1–5, Oct. 2023.

[21] L. Wang, X. L. Peng, H. S. Yang, C. W. Tzeng, J. R. Zhang, and C. C. Tseng, "Stability analysis of a grid-connected large-scale DC microgrid with hybrid wind/solar farm," IET-ICETA, Changhua, Taiwan, pp. 1–2, Oct. 2022.

[22] M. Z. Farooqi, B. Singh, and B. K. Panigrahi, "Modified MPC approach to single-phase two-stage AC–DC

converter," IEEE GlobConPT, New Delhi, India, pp. 1–6, Sept. 2022.

[23] G. Niyitegeka, E. M. Harerimana, G. Park, and J. Choi, "Phase shift modulation and DC-link voltage balancing control for a DAB DC–DC converter," 2018 International Conference on Smart Grid (icSmartGrid), Nagasaki, Japan, pp. 70–75, 2018.

[24] S. Rezayi, H. Iman-Eini, M. Hamzeh, S. Bacha, and S. Farzamkia, "Dual-output DC/DC boost converter for bipolar DC microgrids," IET Renewable Power Generation, vol. 13, no. 8, pp. 1402–1410, June 2019. doi: 10.1049/iet-rpg.2018.6167.

[25] P. Prabhakaran and V. Agarwal, "Novel four-port DC–DC converter for interfacing solar PV–fuel cell hybrid sources," IEEE Journal of Emerging and Selected Topics in Power Electronics, vol. 8, no. 2, pp. 1330–1340, June 2020.

[26] V. F. Pires, D. Foito, A. Cordeiro, C. Roncero-Clemente, and J. F. Silva, "Bidirectional DC–DC converter for battery storage systems," IECON 2022, Brussels, Belgium, pp. 1–6, Oct. 2022.

[27] V. F. Pires, A. Cordeiro, C. Roncero-Clemente, S. Rivera, and T. Dragičević, "DC–DC converters for bipolar microgrid voltage balancing," IEEE Journal of Emerging and Selected Topics in Power Electronics, vol. 11, no. 1, pp. 981–998, Feb. 2023.

[28] Q. Tian, X. Zhang, G. Zhou, X. Wang, B. Guo, and H. Ma, "Symmetrical bipolar output converters based on voltage-multiplying rectifiers," IEEE Transactions on Power Electronics, vol. 38, no. 7, pp. 9157–9172, July 2023.

[29] S. H. Kim, H. J. Byun, W. S. Jeong, J. Yi, and C. Y. Won, "Hierarchical control with voltage balancing and energy management for bipolar DC microgrid," IEEE Transactions on Industrial Electronics, vol. 70, no. 9, pp. 9147–9157, Sept. 2023.

[30] T. Karaipoom and I. Ngamroo, "Enhancement of LVRT performance of DFIG wind turbine in DC microgrid by SMES," IEEE Conference, Beijing, China, pp. 207–208, Oct. 2013.

[31] S. Bayhan, H. Abu-Rub, and O. Ellabban, "Sensorless model predictive control scheme of wind-driven doubly fed induction generator in DC microgrid," IET Renewable Power Generation, vol. 10, no. 4, pp. 514–521, Apr. 2016.

[32] S. M. A. Cruz, G. D. Marques, P. F. C. Gonçalves, and M. F. Iacchetti, "Predictive torque and rotor flux control of a DFIG-DC system," IEEE Transactions on Industrial Electronics, vol. 65, no. 12, pp. 9301–9310, Dec. 2018.

[33] S. Yan, S. Wang, Y. Zhou, X. Sun, and G. Jing, "Study on an optimum design for DC and doubly-controlled DFIG system," Chinese Control and Decision Conference (CCDC), Nanchang, China, pp. 1594–1598, June 2019.

[34] A. Shukla and R. Sharma, "Modified inverter control for DFIG based system on DC microgrid," ICICCS, Madurai, India, pp. 1607–1611, June 2018.

[35] S. H. Khan, L. Saeed, M. Y. Ali Khan, J. Saleem, and A. Majid, "Multiple-input multiple-output bipolar DC–DC voltage gain converter with backup battery port," ICEET, Lahore, Pakistan, pp. 1–6, Feb. 2019.

[36] P. S. Flannery and G. Venkataramanan, "A fault tolerant doubly fed induction generator wind turbine using a parallel grid side rectifier and series grid side converter," IEEE Transactions on Power Electronics, vol. 23, no. 3, pp. 1126–1135, May 2008.

[37] M. Ghodbane-Cherif, S. Skander-Mustapha, and I. Slama-Belkhodja, "An improved predictive control for parallel grid-connected doubly fed induction generator-based wind systems," Wind Engineering, vol. 43, no. 4, pp. 377–391, June 2019.

[38] M. Ghodbane-Cherif, S. Skander-Mustapha, and I. Slama-Belkhodja, "Start-up system design for small scale autonomous DFIG wind turbine," Wind Engineering, vol. 45, no. 4, pp. 753–768, June 2021.

[39] L. Saihi, Y. Bakou, A. Harrouz, M. Boura, I. Colak, and K. Kayisli, "Fuzzy-sliding mode control second order of wind turbine based on DFIG," 2022 International Conference on Smart Grid (icSmartGrid), Istanbul, Turkey, pp. 296–300, 2022.

[40] I. Ngom, A. B. Mboup, L. Thiaw, S. Skander-Mustapha, and I. S. Belkhodja, "An improved control for DC-link fluctuation during voltage dip based on DFIG," 9th International Renewable Energy Congress (IREC), Hammamet, Tunisia, pp. 1–6, Mar. 2018.

[41] Y. E. Abu Eldahab, A. Zekry, and N. H. Saad, "Assessing wind energy conversion systems based on newly developed wind turbine emulator," International Journal of Smart Grid-ijSmartGrid, vol. 4, no. 4, pp. 139–148, Dec. 2020.

## APPENDIX

**Table 2.** BDCMG parameters for simulation

| Wind system | Symbol | Designation | Value |
|---|---|---|---|
| 1 | $P_{Load1}$ | Load rated power (kW) | 720 |
| | $V_{DC1}$ | DC-bus Voltage (V) | 1200 |
| | $V_{r\,WT1}$ | Rated rotor voltage (V) | 2070 |
| | $V_{sWT1}$ | Rated stator voltage (V) | 690 |
| | $P_{WT1}$ | Rated power (kW) | 2000 |
| 2 | $P_{Load2}$ | Load rated power (kW) | 288 |
| | $V_{DC2}$ | DC-bus Voltage (V) | 1200 |
| | $V_{r\,WT2}$ | Rated rotor voltage (V) | 2070 |
| | $V_{sWT2}$ | Rated stator voltage (V) | 690 |
| | $P_{WT2}$ | Rated power (kW) | 2000 |

**Table 3**. BDCMG parameters for PHIL experiment validation

| Wind system | Symbol | Designation | Value |
|---|---|---|---|
| 1 | $V_{DC1}$ | DC-bus Voltage (V) | 450 |
| | $V_{r\,WT1}$ | Rated rotor voltage (V) | 307 |
| | $V_{sWT1}$ | Rated stator voltage (V) | 400 |
| | $P_{WT1}$ | Rated power (kW) | 3,730 |
| 2 | $V_{DC2}$ | DC-bus Voltage (V) | 450 |
| | $V_{r\,WT2}$ | Rated rotor voltage (V) | 307 |
| | $V_{sWT2}$ | Rated stator voltage (V) | 400 |
| | $P_{WT2}$ | Rated power (kW) | 3,730 |

**Table 4.** Analysis of system response with different control

| **Wind system** | **Converter** | **Control** | **Value** | **Ripples (%)** | **Value** | **Ripples (%)** |
|---|---|---|---|---|---|---|
| **1** | RsC | Predictive | $i_{rq}$ | 2% | *Torque* | 8% |
| **2** | | PI | | 20% | | 30% |
| **Wind system** | **Converter** | **Control** | **Value** | **THD** | | |
| **1** | SsC | Predictive | $i_s$ | 4.77% | | |
| **2** | | RC | | 10,26% | | |